Colloid Polym Sci (2004) 283: 265–276
DOI 10.1007/s00396-004-1124-1

ORIGINAL CONTRIBUTION

C. Giordano
A. Longo
A. Ruggirello
V. Turco Liveri
A. M. Venezia

Physicochemical investigation of cobalt–iron cyanide nanoparticles synthesized by a novel solid–solid reaction in confined space

Received: 19 December 2003
Accepted: 22 March 2004
Published online: 24 April 2004

C. Giordano · A. Ruggirello
V. Turco Liveri (✉)
Department of Physical Chemistry,
Università di Palermo, Viale delle Scienze
Parco D'Orleans II, 90123 Palermo, Italy
E-mail: turco@unipa.it

A. Longo · A. M. Venezia
ISMN, Istituto per lo Studio dei Materiali
Nanostrutturati, Via U. La Malfa 153,
90146 Palermo, Italy

Abstract Cobalt–iron cyanide ($Co_x[Fe(CN)_6]$) nanoparticles have been synthesized by a novel solid–solid reaction in the confined space of dry sodium bis(2-ethylhexyl)sulfosuccinate (AOT) reversed micelles dispersed in *n*-heptane. The reaction has been carried out by mixing two dry AOT/*n*-heptane solutions containing $CoCl_2$ and $K_4Fe(CN)_6$ or $K_3Fe(CN)_6$ nanoparticles in the micellar core, respectively. By UV-Vis spectroscopy it was ascertained that, after the mixing process, the formation of stable nanoparticles is fast and complete. Microcalorimetric measurements of the thermal effect due to the $Co_x[Fe(CN)_6]$ nanoparticle formation allowed the determination of the stoichiometric ratio (x) and of the molar enthalpy of reaction in the core of AOT reversed micelles. The observed behavior suggests the occurrence of confinement effects and surfactant adsorption on the nanoparticle surface. Further structural information was achieved by small-angle X-ray scattering (SAXS) measurements. From all liquid samples, interesting salt/AOT composites were prepared by simple evaporation of the apolar solvent. Size, crystal structure, and electronic properties of $Co_x[Fe(CN)_6]$ nanoparticles containing composites were obtained by wide-angle X-ray scattering (WAXS) and X-ray photoelectron spectroscopy (XPS).

Keywords Cobalt–iron cyanide complexes · Nanoparticles · Solid–solid reaction · Confinement effect · AOT reversed micelles

Introduction

Solid-state reactions are generally very slow processes as a consequence of the negligible diffusion rate of chemical species in solids. To circumvent this drawback, the most frequently used expedient is to employ finely milled powders and to increase the temperature up to 1,000–1,500°C. However, recently the use of nanoparticle dispersions in reversed micellar solutions has been suggested as a novel route allowing fast solid-state reactions without the need for drastic and economically disadvantageous working conditions [1, 2].

In particular, for the synthesis of inorganic salts, the proposed method consists of the following steps: i) entrapment of appropriate amounts of the selected reagent salt in the hydrophilic core of the water-containing reversed micelles dispersed in apolar solvent, ii) complete evaporation of volatile components (water and apolar solvent) of the salt-containing system, iii) resuspension of the salt/surfactant composite in apolar solvent leading to the formation of dry dispersions of salt nanoparticles coated by opportunely oriented surfactant molecules [3, 4], and iv) mixing of two appropriate dry dispersions of nanoparticle containing reversed micelles.

During the last step, reactant nanoparticles can easily come into contact and quickly react to form product nanoparticles, as a consequence of the very high surface-to-volume ratio of nanoparticles and of the fast intermicellar material exchange process. By using this method, the fast and complete synthesis of small-sized ZnS, AgCl, and AgBr nanoparticles steadily dispersed in AOT/*n*-heptane solutions has been achieved [1, 2]. It has been also shown that a fine size control of these nanoparticles can be obtained by the optimisation of some external parameters such as precursor and surfactant concentrations.

Given the typical superparamagnetic behavior of magnetic nanoparticles and the importance of cobalt–iron cyanide salts as promising candidates for the next generation of magnets [5] with potential for a variety of applications (e.g., as magneto-optical devices, magnetocaloric refrigeration, and drug delivery [6]), we undertook an investigation aiming to set up a suitable synthetic protocol of these materials by the abovementioned procedure and to characterize their physicochemical properties**.** In particular, the synthesis of cobalt–iron cyanide complex nanoparticles was carried out by mixing two AOT/*n*-heptane solutions at a fixed surfactant concentration ([AOT] = 0.071 mol dm^{-3}), one containing $CoCl_2$ and the other $K_4Fe(CN)_6$ or $K_3Fe(CN)_6$.

Experimental

Materials

Sodium bis(2-ethylhexyl)sulfosuccinate (aerosol-OT, AOT Sigma 99%) was stored in a desiccator and used after at least one week. *n*-Heptane (Aldrich 99% spectrophotometric grade), cobalt chloride hexahydrate (Sigma, ACS reagent), potassium hexacyanoferrate(II) trihydrate, and potassium hexacyanoferrate(III) were used as received. Doubly distilled water was used in all experiments.

Methods

Water/AOT/*n*-heptane w/o microemulsions were prepared at various water-to-AOT molar ratios (*W*s) by adding the appropriate amount of water to a weighed quantity of AOT/*n*-heptane solution at fixed surfactant concentration ([AOT] = 0.071 mol dm^{-3}).

Salt-containing w/o microemulsions with various salt-to-AOT molar ratios (*R*), were prepared by adding the appropriate amount of w/o microemulsion to a weighed quantity of salt. An ultrasonic bath was employed to speed up the solubilization of the salts within the aqueous core of AOT reversed micelles. At each *W* value, the solubility of $CoCl_2 \cdot 6\ H_2O$, $K_4Fe(CN)_6 \cdot 3\ H_2O$, and $K_3Fe(CN)_6$ in w/o microemulsions was determined by visual inspection of samples prepared at various *R* values and kept at constant temperature (25°C). These data, expressed as the maximum value of the salt-to-AOT molar ratio (R_{max}) and of the moles of salt per kilogram of water ($[salt]_w$), are reported in Table 1. To check their stability, UV-Vis spectra of these samples were collected as a function of time. An analysis of the time dependence of these spectra allowed us to put into evidence the occurrence of some minor spectral changes of the $K_4Fe(CN)_6$- and $K_3Fe(CN)_6$-containing w/o microemulsions. However, these changes, attributable to the occurrence of secondary redox reactions, become visually evident at least two weeks after their preparation. For this reason, all the experiments were carried out using freshly prepared samples.

Evaporation of volatile components of freshly prepared salt-containing w/o microemulsions was achieved by means of a desiccator connected to a diaphragm vacuum pump (MZ2C, Vacuubrand). To avoid effects arising from the evaporation rate, the same experimental conditions have been used, that is, initial amount of sample (5 g), shape and volume of sample container (25-cm^3 bottle), and operational temperature (20 ± 2°C). Under these conditions, complete evaporation of the volatile components occurs in about 1 h. However, all

Table 1 Solubility of $CoCl_2 \cdot 6\ H_2O$, $K_4Fe(CN)_6 \cdot 3\ H_2O$, and $K_3Fe(CN)_6$, expressed as salt-to-AOT molar ratio (R_{max}) and moles of salt per kilogram of water ($[salt]_w$), in water/AOT/n-heptane ([AOT] = 0.071 mol dm^{-3}) microemulsions at various water-to-AOT molar ratios (*W*) and in pure water

Salt/water/AOT/*n*-heptane						
W	R_{max}	$[CoCl_2]_w$	R_{max}	$[K_4Fe(CN)_6]_w$	R_{max}	$[K_3Fe(CN)_6]_w$
3	0.046	0.85	0.009	0.16	0.025	0.46
5	0.136	1.51	0.028	0.31	0.053	0.59
8	0.088	0.61	0.051	0.35	0.069	0.48
10	0.054	0.30	0.020	0.11	0.045	0.25
Pure water		1.45[a]		0.66[b]		1.40[b]

[a]Ref. [10]
[b]Ref. [11]

salt–surfactant composites were subsequently maintained under vacuum at least for 2 h.

Complete dispersion of the dry salt/surfactant composites in apolar solvent was achieved by adding the appropriate amount of pure *n*-heptane to obtain the initial AOT concentration. The stability of $CoCl_2$/AOT, $K_4Fe(CN)_6$/AOT, and $K_3Fe(CN)_6$/AOT composite dispersions was checked over a long time (several months). No significant change of their UV-Vis spectra was observed. It must be noted that dry dispersions show an enhanced stability with respect to salt-containing w/o microemulsions. Moreover, even if water is virtually absent in the resuspended composites, a considerable amount of salts can be steadily dispersed in an apolar medium.

The solid–solid reactions in confined space were performed at 25°C by mixing two dry AOT/*n*-heptane solutions, one containing $CoCl_2$, and the other $K_4Fe(CN)_6$ or $K_3Fe(CN)_6$. The amounts of these solutions were chosen to obtain the desired molar ratio (S) of $CoCl_2$ to $K_4Fe(CN)_6$ or $K_3Fe(CN)_6$. Immediately after the mixing process, a color change is observed while the solutions remain clear and stable for long periods (at least one month).

UV-Vis-NIR spectra were recorded in the wavelength range 200–2,200 nm with a Perkin–Elmer (Lambda-900) spectrophotometer.

Calorimetric measurements were carried out at 25°C with a thermal activity monitor (LKB) equipped with a flow-mix cylinder (LKB 2277–204). As a standard procedure, two dry AOT/*n*-heptane solutions at the same surfactant concentration ([AOT] = 0.071 mol dm^{-3}), one containing $CoCl_2$, and the other $K_4Fe(CN)_6$ or $K_3Fe(CN)_6$, were driven by two peristaltic pumps (Gilson, Minipulse 2) into the calorimetric cell where the reaction took place, and the flow rates were measured by weight. The desired S value was obtained by changing the flow rate ratio (ϕ_1/ϕ_2) of the two peristaltic pumps. Moreover, the total flow rate ($\phi_1 + \phi_2$) was chosen to assure the occurrence of the totality of the thermal effect inside the calorimeter cell ($\phi_1 + \phi_2 \leq 10^{-2}$ g s^{-1}) in all cases. Baseline was determined by mixing two dry AOT/*n*-heptane solutions at [AOT] = 0.071 mol dm^{-3}. Preliminary experiments showed that the thermal effect due to dilution of $CoCl_2$-, $K_4Fe(CN)_6$- and $K_3Fe(CN)_6$-containing AOT/*n*-heptane solutions is negligible. The experimental molar enthalpy (ΔH) of the cobalt–iron cyanide nanoparticle formation inside AOT reversed micelles was calculated by using the following equation:

$$\Delta H = Q/n_{\mathrm{Fe(II\ or\ III)}} \tag{1}$$

where Q is the thermal power (kJ s^{-1}) and $n_{\mathrm{Fe(II\ or\ III)}}$ is the flux (mol s^{-1}) of Fe(II) or Fe(III) moles entering inside the calorimetric cell [2].

Small-angle X-ray scattering (SAXS) patterns have been recorded by a laboratory instrumentation consisting of a Philips PW 1830 X-ray generator providing Cu Kα, Ni-filtered ($\lambda = 1.5418$ Å) radiation with a Kratky small-angle camera in the "finite-slit-height" geometry equipped with step scanning motor and scintillation counter. Each scattering spectrum of freshly prepared samples was subtracted by the cell and solvent contributions. The data were analyzed by using the CERN minimization program called MINUITS. Considering that in our experimental conditions inter-particle interactions can be neglected, fitting of the SAXS spectra was performed by using the following equation:

$$I(q) \propto \int_{-\infty}^{+\infty} P(t)\langle F(q,t)\rangle^2 dt \tag{2}$$

where q is the elastic scattering vector, $\langle F(q,t)\rangle$ is the form factor of the scattering centers, t is a variable defined along the length of the line-shaped primary X-ray beam, and $P(t)$ is its intensity distribution function [7]. The form factor $\langle F(q,t)\rangle$ depends on the shape of the scattering centers and was varied by considering three different models: polydisperse spheres, monodisperse cylinders, and monodisperse ellipsoids [8]. The standard deviation was taken as a probe of the goodness of the fit.

X-ray powder diffraction spectra of composites were measured by using a Philips diffractometer (PW1050/39 X Change) equipped with a copper anode (Cu Kα, $\lambda = 1.5418$ Å).

The X-ray photoelectron spectroscopy (XPS) analysis was carried out with a VG Microtech ESCA 3000 Multilab, equipped with a dual Mg/Al anode. The spectra were excited by the non-monochromatised Al Kα source (1,486.6 eV) run at 14 kV and 15 mA. The analyzer operated in the constant-analyzer-energy mode. Survey spectra were measured at 50-eV pass energy. For the individual peak energy regions, the pass energy of 20 eV set across the hemispheres was used, except for cobalt–iron cyanide complex/AOT composites (given the low intensity of the peaks) for which a 50-eV pass energy was used. The composites were pelletized and then mounted on double-sided adhesive tape. The pressure in the analysis chamber was approximately 10^{-8} Torr during data collection. The constant charging of the samples was removed by referencing all the energies to the C 1*s* at 285.1 eV, arising from the adventitious carbon. The invariance of the peak shapes and widths at the beginning and end of the analyses indicated absence of differential charging. The binding energy (BE) values are quoted with a precision of ±0.15 eV.

Results and discussion

Solubility

The solubility of $CoCl_2 \cdot 6\ H_2O$, $K_4Fe(CN)_6 \cdot 3\ H_2O$, and $K_3Fe(CN)_6$ in water/AOT/*n*-heptane microemulsions,

expressed as the maximum salt-to-AOT molar ratio (R_{max}), is shown as a function of W ($W = [H_2O]/[AOT]$) in Fig. 1. The observed W-dependence of the solubility, similar to that of Na_2S, $ZnSO_4$, and $Co(NO_3)_2 \cdot 6\ H_2O$ previously found [4, 9], can be rationalized in terms of two opposite factors: i) the saturation of the aqueous micellar core, predominant at low W, leading to an increase of R_{max}; and ii) the salt effect on the solubility of water in AOT micellar solutions, predominant at high W, determining a decrease of the water solubility and consequently of R_{max} [4, 10, 11]. The concurrence of both effects leads to a maximum value of R_{max} and of the moles of salt per kilogram of water ($[salt]_w$) at about $W = 5$–8. It is of interest to compare the salt solubility in water/AOT/*n*-heptane microemulsions with that in pure water (see Table 1) [12, 13].

Apart from the $[CoCl_2]_w$ value at $W = 5$, it can be noted that the solubility of all salts in water/AOT/*n*-heptane microemulsions is lower than that in pure water. This behavior can be rationalized in terms of the salting out effect resulting from the contemporaneous presence of AOT sodium counterions in the micellar core and/or to confinement effects. On the other hand, the "anomalous" behavior of $CoCl_2$ can be attributed to a side effect of the metathesis reaction between $CoCl_2$ and AOT occurring at the water/surfactant interface and leading to the formation of the stable Co(II)/AOT complex and the release in the micellar core of sodium counterions [9].

UV-Vis-NIR spectra

Typical UV-Vis-NIR spectra of $CoCl_2$-, $K_4Fe(CN)_6$-, and $K_3Fe(CN)_6$-containing water/AOT/*n*-heptane microemulsions in the 200–2,200 nm wavelength range are shown in Fig. 2. For comparison, the spectrum of AOT/*n*-heptane solution at the same AOT concentration is also reported.

Concerning the spectra of $CoCl_2$-containing water/AOT/*n*-heptane microemulsions, we observed the band occurring at about 516 nm owing to the spin-allowed d–d transition from the ground state, $^4T_{1g}(F)$, to the $^4T_{1g}(P)$ state of the octahedrally coordinated cobalt(II) cation [14, 15]. Apart from some changes of the band position with W (522.4 nm at $W = 3$, 516.9 nm at $W = 5$, and 511.6 nm at $W = 8$), it must be noted that it is close to that of $CoCl_2$ in bulk water (511.5 nm), tending to it at high W. The deviations of the band position with respect to that in bulk water can be reasonably attributed to effects due to a change in the nature of the Co(II) ligands (i.e., water molecules are more or less extensively substituted by AOT head groups) [9]. This implies that some sodium counterions are removed from the water/AOT interface and pushed toward the interior of the micellar core.

On the other hand, the spectra of $K_4Fe(CN)_6$-containing water/AOT/*n*-heptane microemulsions are characterized by the presence of a band occurring at

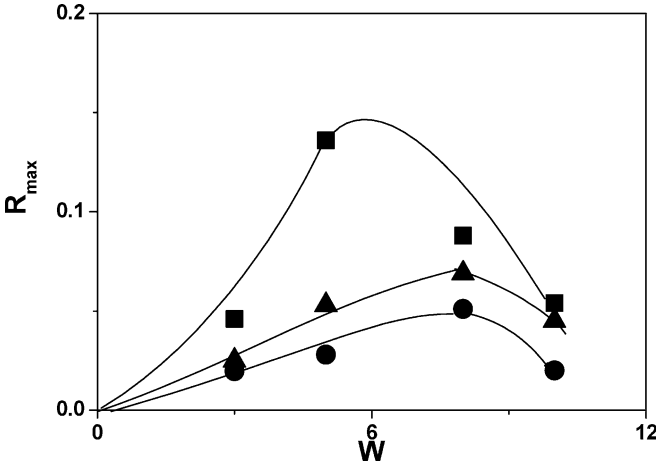

Fig. 1 Solubility (R_{max}) of $CoCl_2 \cdot 6\ H_2O$ (■), $K_4Fe(CN)_6 \cdot 3\ H_2O$ (●), and $K_3Fe(CN)_6$ (▲) in water/AOT/*n*-heptane microemulsions as a function of W

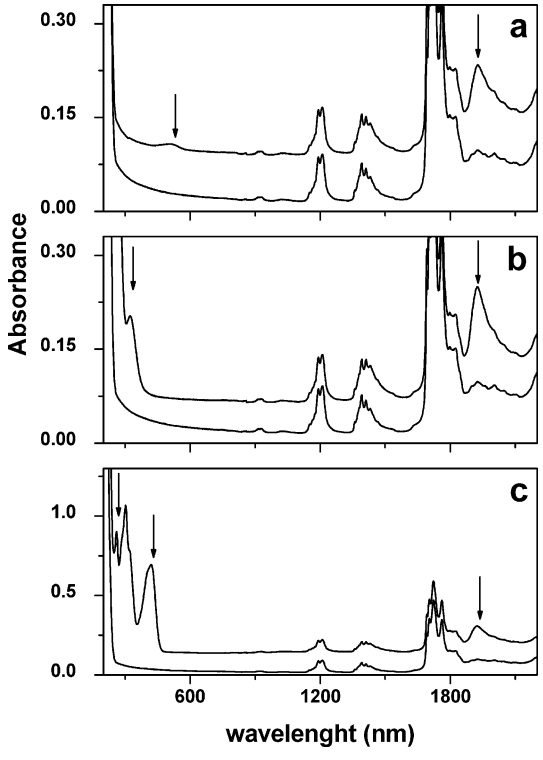

Fig. 2a–c UV-Vis-NIR spectra of **a** $CoCl_2$- ($W = 5.0$, $R = 0.136$), **b** $K_4Fe(CN)_6$- ($W = 8.0$, $R = 0.051$), and **c** $K_3Fe(CN)_6$- ($W = 8.0$, $R = 0.069$) containing water/AOT/*n*-heptane system ($[AOT] = 0.071$ mol dm^{-3}). In all the *panels*, the *lower spectrum* refers to the AOT/*n*-heptane system at the same surfactant concentration

about 320 nm, which has been tentatively attributed to the d–d transition from $^1A_{1g}$ to the $^1T_{1g}$ state of the coordinated Fe(II) cation [16]; whereas those of $K_3Fe(CN)_6$-containing water/AOT/*n*-heptane microemulsions display bands at about 260, 300, and 420 nm attributed to charge-transfer transitions from the cyanide ligand to the Fe(III) cation [17]. No significant changes of the position of these bands as a function of W as well with respect to that in bulk water were observed. These findings indicate that confinement in water-containing AOT reversed micelles of Fe(II) and Fe(III) complex salts does not involve changes on their first coordination shell. Moreover, in all the spectra, it occurs a band at about 1,920 nm due to a combination mode of stretching and bending vibrations of water [18, 19]. This band allows one to evaluate the amount of water encapsulated in the AOT reversed micelles. In particular, we have found a quite linear relationship between W and the absorbance at the band maximum. This relationship was used to check the W values in all the investigated samples.

Typical UV-Vis-NIR spectra of the $CoCl_2$/AOT, $K_4Fe(CN)_6$/AOT, and $K_3Fe(CN)_6$/AOT composites resuspended in *n*-heptane ([AOT] = 0.071 mol dm^{-3}) in the 200–2,200 nm wavelength range are shown in Fig. 3. For comparison, the spectra of the corresponding salt-containing water/AOT/*n*-heptane microemulsions, from which the resuspended composites were obtained, are also shown. The absence of band occurring at 1,920 nm in the spectra of the resuspended composites ensures the total absence of water. An analysis of these spectra leads to the following conclusions:

i) the wavelength at the band maximum of the Co(II) ions is the same for all the samples (685 nm) but, most importantly, it changes dramatically with respect to that in water-containing microemulsions. This finding is visually emphasized by the change of the solution color from pale pink to intense blue. A strong enhancement of the band efficiency is also observed. These features indicate that, in resuspended composites, Co(II) ions are tetrahedrally coordinated mainly by Cl^- anions [15]
ii) the band intensity of the Fe(II) and Fe (III) salts and the wavelength at the band maximum do not show significant changes with respect to that in water-containing microemulsions. This indicates that, in resuspended composites, these ions retain the same coordination shell as well as the nature of the ligands.

Figure 4 shows typical UV-Vis spectra of samples at $S = 1$ prepared by mixing two appropriate amounts of dry AOT/*n*-heptane solutions: one containing $CoCl_2$, and the other $K_4Fe(CN)_6$ or $K_3Fe(CN)_6$. The spectra of $CoCl_2$/AOT and $K_4Fe(CN)_6$/AOT or $K_3Fe(CN)_6$/AOT resuspended composites are reported in the same figure for reference. It can be noted that the spectra of the

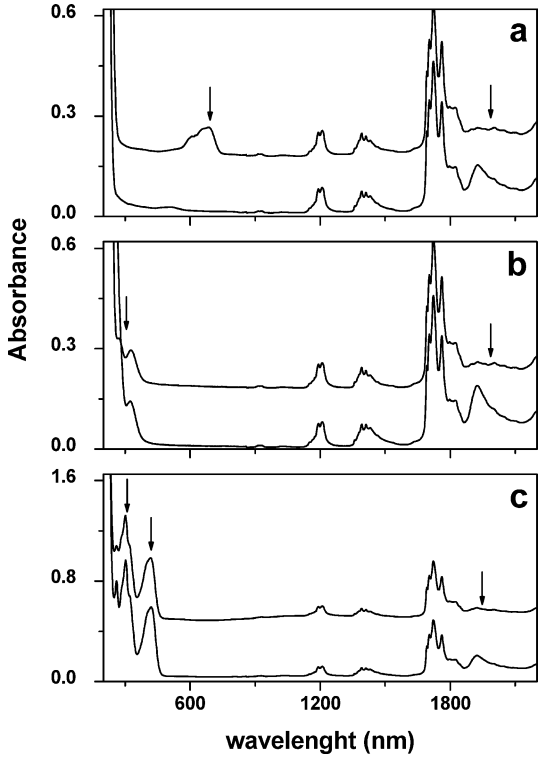

Fig. 3a–c UV-Vis-NIR spectra of **a** $CoCl_2$- ($R = 0.136$), **b** $K_4Fe(CN)_6$- ($R = 0.051$), and **c** $K_3Fe(CN)_6$- ($R = 0.069$) containing AOT/*n*-heptane system ([AOT] = 0.071 mol dm^{-3}). In all the *panels*, the *lower spectrum* refers to the corresponding salt-containing water/AOT/*n*-heptane microemulsions at the same surfactant concentration and at $W = 5$ (**a**) and $W = 8$ (**b**, **c**)

mixtures, recorded immediately after the mixing process, show some significant changes in the intensity and position of the bands with respect to that of the reactant salts in dry reversed micelles, suggesting that some variations of the metal coordination shell occur. On the other hand, no significant spectral changes are observed with time. These findings can be taken as an indication of the fast and complete formation of cobalt–iron cyanide complex nanoparticles.

Calorimetric measurements

Further information on the formation of cobalt iron complex nanoparticles confined in AOT reversed micelles have been achieved by microcalorimetric measurements of the thermal power (Q) occurring when two reactant-containing reversed micellar solutions are mixed inside the calorimetric cell as a function of the flux of moles ($n_{Co(II)}$ and $n_{Fe(II)}$ or $n_{Fe(III)}$) of the reactants. Typical trends of the experimental data, reported as $Q/n_{Fe(II\ or\ III)}$ versus $n_{Co(II)}/n_{Fe(II\ or\ III)}$, are shown in Fig. 5. It can be noted that an initial linear increase, corresponding to a condition in which iron ions are in

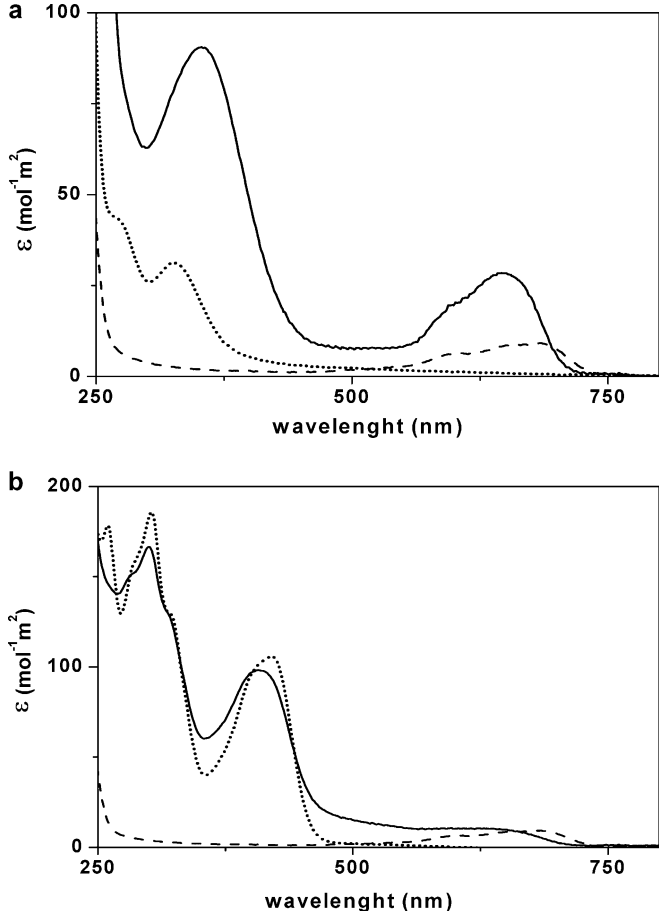

Fig. 4 **a** UV-Vis spectra of salt-containing AOT/*n*-heptane systems. $CoCl_2$/AOT/*n*-heptane at $R = 0.037$ (*dashed line*), $K_4Fe(CN)_6$/AOT/*n*-heptane at $R = 0.030$ (*dotted line*), and $CoCl_2 + K_4Fe(CN)_6$ at $S = 1$ (*continuous line*). **b** UV-Vis spectra of salt-containing AOT/*n*-heptane systems. $CoCl_2$/AOT/*n*-heptane at $R = 0.037$ (*dashed line*), $K_3Fe(CN)_6$/AOT/*n*-heptane at $R = 0.030$ (*dotted line*), and $CoCl_2 + K_3Fe(CN)_6$ at $S = 1$ (*continuous line*)

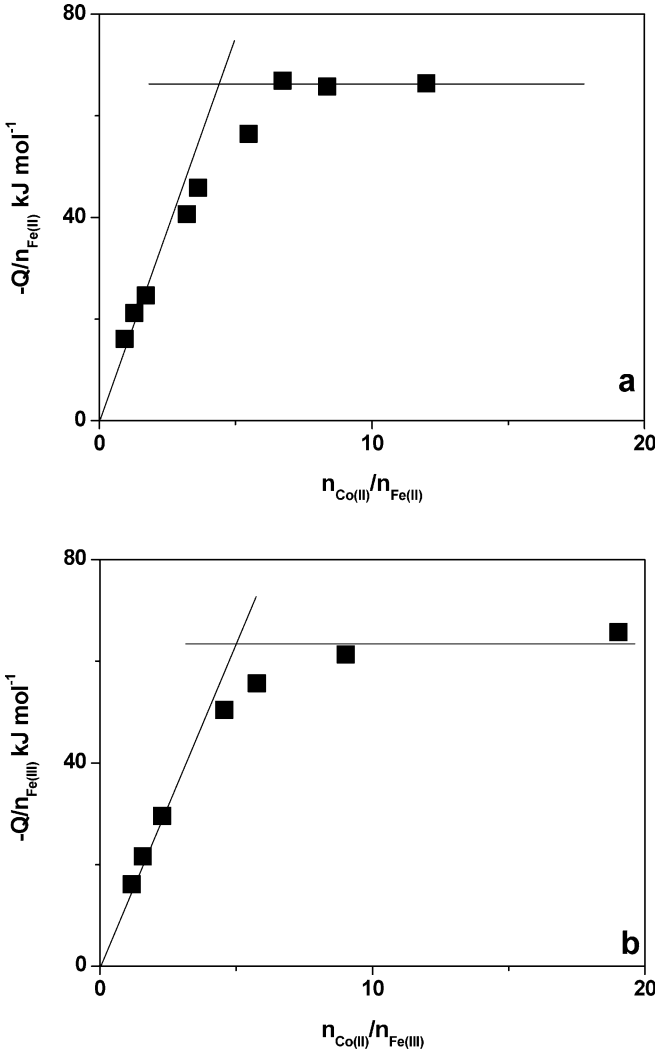

Fig. 5a,b Experimental molar enthalpy ($Q/n_{Fe(II\ or\ III)}$, kJ mol^{-1}) as a function of the flux mole ratio $n_{Co(II)}/n_{Fe(II\ or\ III)}$ for the formation of **a** cobalt–iron(II) ($R_{Co(II)} = 0.051$ and $R_{Fe(II)} = 0.044$) and **b** cobalt–iron(III) ($R_{Co(II)} = 0.083$ and $R_{Fe(III)} = 0.051$) cyanide complex nanoparticles

excess, is followed by a constant trend where they are in deficit. The plateau value then indicates the molar enthalpy of formation of cobalt–iron cyanide nanoparticles, while the intersection point between the two trends allows the evaluation of the stoichiometric ratio (x) of the $Co_x[Fe(CN)_6]$ complexes. An analysis of all the experimental data shows that, quite independently of the R values ($0.03 \le R \le 0.08$), the molar enthalpy of formation of the cobalt–iron(II) cyanide complexes is -67.9 ± 1.5 kJ mol^{-1} and the x value is 5.7 ± 0.3, while the corresponding values of the cobalt–iron(III) cyanide complexes are -63.4 ± 2.5 kJ mol^{-1} and $x = 5.1 \pm 0.4$. It must be noted that the x values do not correspond to the stoichiometric ratio expected according to the cobalt/ligand valencies. This could be attributed to confinement effects and surfactant adsorption on the nanoparticle surface.

Concerning the values of the molar enthalpies of formation of cobalt–iron cyanide nanoparticles, it must be stressed that experimental data on the energetics of solid–solid reactions in microheterogeneous systems are absent in the literature, so that these data are the first reported ones and could be used as a test standard for theoretical calculations.

SAXS Spectra

Small-angle X-ray scattering data of the $CoCl_2$/AOT ($R = 0.076$), $K_4Fe(CN)_6$/AOT ($R = 0.049$), and $K_3Fe(CN)_6$/AOT ($R = 0.062$) resuspended composites are shown in Fig. 6. For comparison the spectrum of

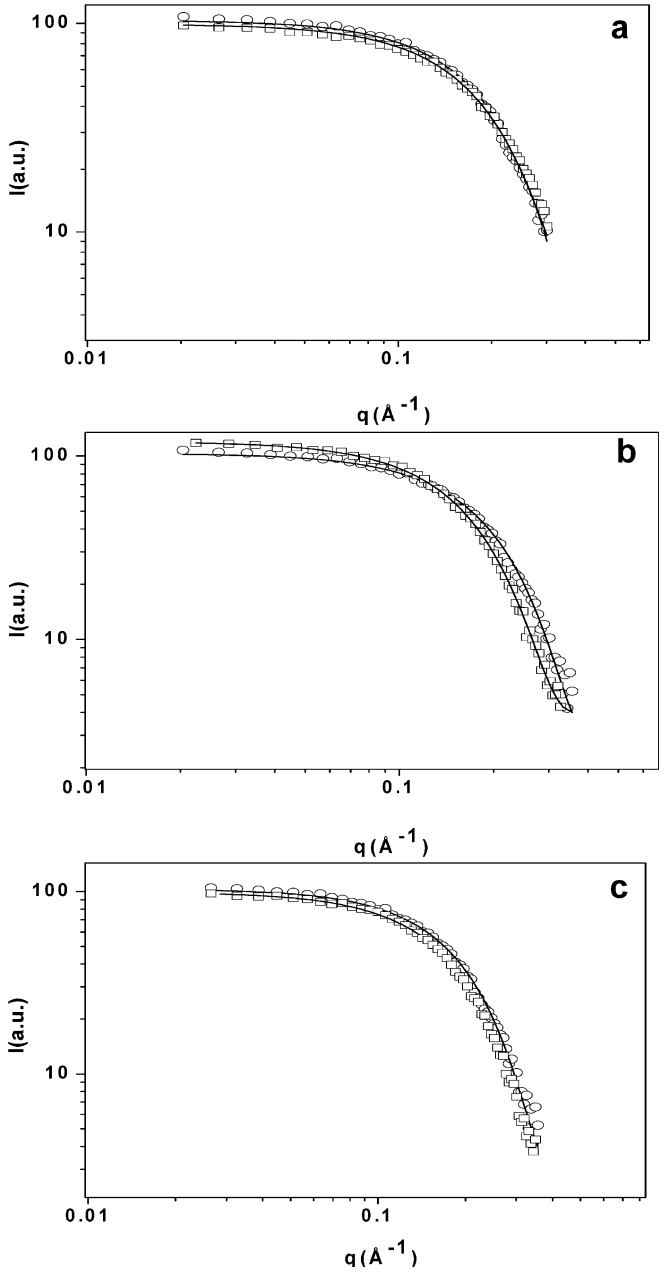

Fig. 6a–c Typical smeared scattering profiles and fittings of resuspensions of **a** $CoCl_2$/AOT/*n*-heptane ($R=0.076$), **b** $K_4Fe(CN)_6$/AOT/*n*-heptane ($R=0.049$), and **c** $K_3Fe(CN)_6$/AOT/*n*-heptane ($R=0.062$) (□) and of AOT/*n*-heptane solution (○)

AOT/*n*-heptane system at the same surfactant concentration is also reported. All these SAXS spectra were adequately described by a model of non-interacting, polydisperse homogenous scattering spheres with a size distribution described by the function $N(r)$, where r is the sphere radius. Since small-angle X-ray scattering is due to the contrast between regions with different electron densities, and considering the reversed micelle structure, the scattering spheres of the model are to be interpreted as the bare or salt-containing micellar cores [20, 21].

The derived parameters, obtained by following the procedure described elsewhere [1], are the micellar core mean radius (r_m) and the parameter b, which is a quantitative descriptor of the size polydispersity. These parameters are collected in Table 2, and the size distribution functions of the core of bare and salt-containing AOT reversed micelles are shown in Fig. 7.

It is noteworthy that the mean radius of the micellar core at $R=0$ ($r_m=10.8$ Å) is in good agreement with the literature value ($r_m=9.4$ Å) for AOT micelles in *n*-decane [22]; the difference could be due to the presence of water trace and/or to the nature of the apolar medium.

A perusal of Table 2 reveals that the micellar core mean radius increases slightly in the presence of reactant salts. In contrast, the corresponding b values show a marked decrease involving a significant increase of the particle size polydispersity. These findings indicate that the reactant salts are localized as very small nanoparticles in the micellar core of some AOT reversed micelles. In fact, the entrapment of salt as small nanoparticles within some reversed micelles causes an increase of their core size and surfactant aggregation number. This means that the concentration of the remaining bare AOT reversed micelles decreases leading to an increase in their polydispersity. As a result of both effects, the overall polydispersity increases [23].

SAXS spectra of the cobalt–iron cyanide complex containing AOT reversed micelles are compared with that of the AOT/*n*-heptane system in Fig. 8. A good fitting of these spectra was achieved by a model of bimodal distribution of polydisperse spheres. The fitting parameters are shown in Table 2, and the size distribution functions of the core of cobalt–iron cyanide complex containing AOT reversed micelles are shown in Fig. 9. It is of interest to note that, in addition of small

Table 2 Mean radius (r_m) and b values of the core of bare and salt-containing AOT reversed micelles dispersed in *n*-heptane

Sample	r_{m1}(Å) ± 0.5	b_1 ± 0.2	r_{m2}(Å) ± 0.5	b_2 ± 0.2
Pure AOT	10.8	18.6		
$CoCl_2$/AOT ($R_s=0.076$)	11.0	10.0		
$K_4Fe(CN)_6$/AOT ($R_s=0.049$)	12.4	8.5		
$K_3Fe(CN)_6$/AOT ($R_s=0.062$)	11.5	7.5		
Cobalt–iron(II) cyanide complex/AOT ($S=1$)	11.7	5.6	40.0	6.5
Cobalt–iron(III) cyanide complex/AOT ($S=1$)	13.0	9.2	44.5	6.4

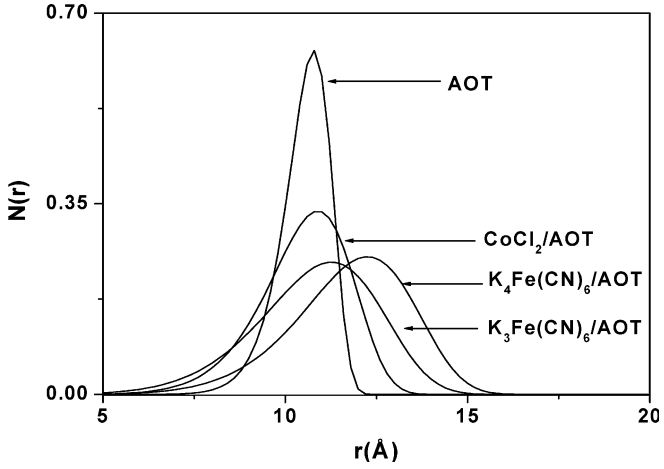

Fig. 7 Size distribution functions of the bare and salt-containing AOT micellar core: $CoCl_2$/AOT ($R=0.076$), $K_4Fe(CN)_6$/AOT ($R=0.049$), $K_3Fe(CN)_6$/AOT ($R=0.062$)

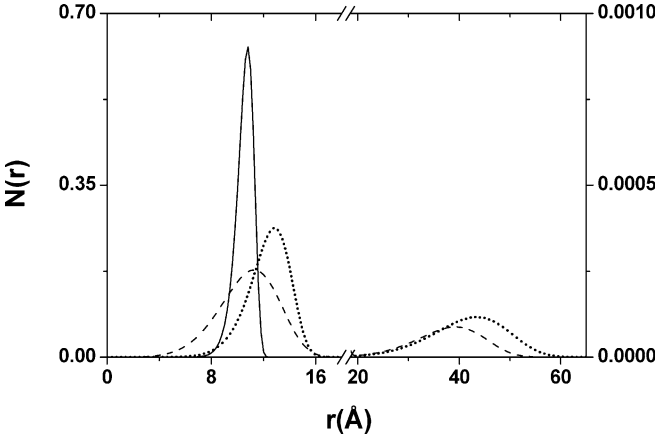

Fig. 9 Size distribution functions of the AOT micellar core containing cobalt–iron(II) (*dashed line*) or cobalt–iron(III) (*dotted line*) cyanide complex nanoparticles and that of bare AOT reversed micelles (*continuous line*)

polydisperse cobalt–iron cyanide complex nanoparticles entrapped in the AOT micellar cores, the appearance of a small fraction of AOT reversed micelles showing a noticeable increase of their core size is also observed. This finding reveals that a rapid solid–solid reaction leading to the formation of small-sized nanoparticles is followed by a slow growing process.

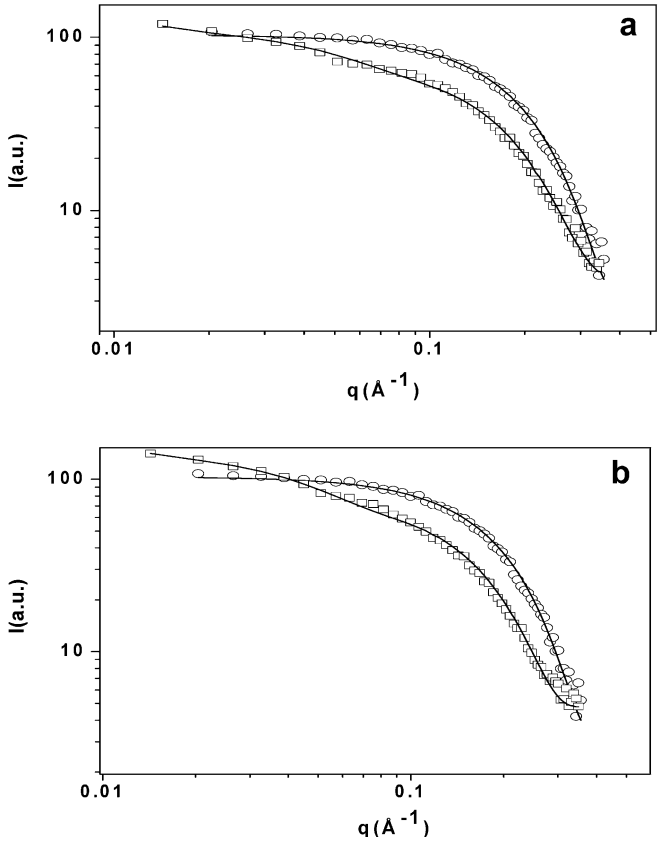

Fig. 8a,b Smeared scattering profiles and fitting curves of **a** $CoCl_2+K_4Fe(CN)_6$ ($S=1$) and **b** $CoCl_2+K_3Fe(CN)_6$ ($S=1$) (□) in AOT/*n*-heptane and of AOT/*n*-heptane solution (○)

WAXS spectra

In view of the potential applications of nanoparticle/surfactant composites, the dispersions of salt-containing reversed micelles were evaporated under vacuum. Typical X-ray powder diffraction spectra of the resulting reactant–salt/AOT composites are compared to that of pure AOT and salts in Fig. 10. In pure AOT as well as in the composite spectra, an intense peak occurs at about $2\theta=4°$, and two other very small peaks at about $2\theta=7°$ and 8° owing to the typical two-dimensional hexagonal structure of AOT liquid crystals [24].

A broad peak at about $2\theta=19.5°$ owing to the amorphous domain formed by the surfactant tails can be also observed. The peak positions and the relative lattice parameters of pure AOT and salt/AOT composites are collected in Table 3, and a schematic representation of the structure of AOT liquid crystals is shown in Fig. 11 [24].

A perusal of the lattice parameters of Table 3 suggests a slight increase of the cross-section of the AOT rods in the presence of the salts, emphasizing that these substances are entrapped in the hydrophilic cores of the hexagonal AOT rods. Moreover, the widening of the broad peak at about $2\theta=19.5°$, suggests that salts induce an increase of the structural disorder in the AOT liquid crystals. On the other hand, the absence of the peaks observed in the pure salts indicates that very small and/or quite amorphous salt nanoparticles are present in salt/surfactant composites.

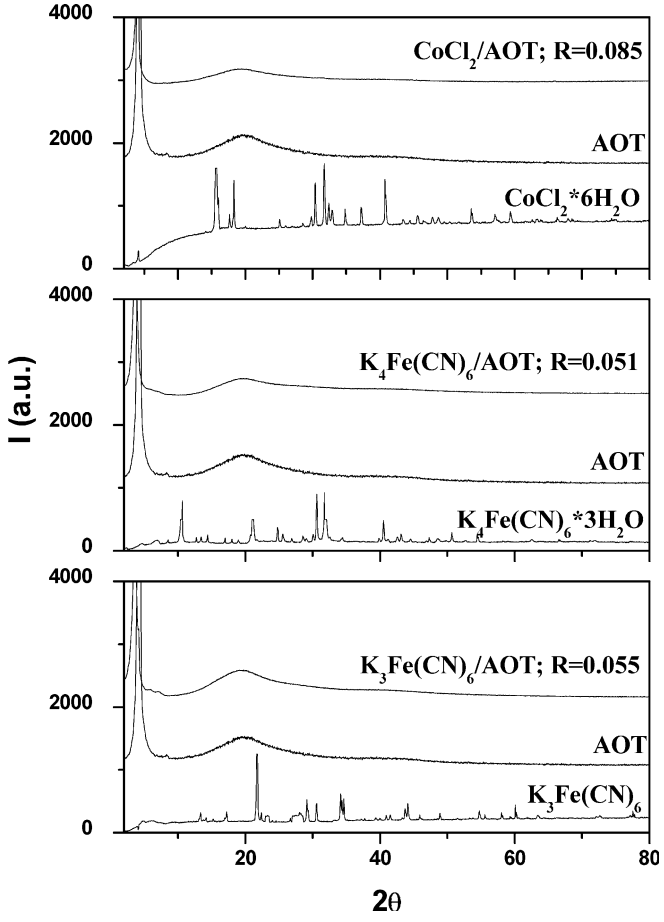

Fig. 10 Comparison between X-ray diffraction spectra of salt/AOT composites with those of pure AOT and reactant salts

X-ray powder diffraction spectra of cobalt–iron complex/AOT composites are shown in Fig. 12. A very small change of the d_{100} parameter (see Table 3) and, most importantly, the appearance of diffraction peaks clearly due to the cobalt–iron cyanide complexes can be noted. This finding indicates that such complexes are in crystalline form embedded within the AOT structure. A rough estimate of the crystal diameter (d) was achieved by using Scherrer's equation leading to a value of about 40 nm, which is much higher than that found in liquid samples, both for cobalt–iron(II) and cobalt–iron(III) cyanide complexes. This finding suggests that during the evaporation process there is a marked growth of nanoparticles attributable to the progressive increase of their concentration in the samples and consequently an increase of the coalescence probability.

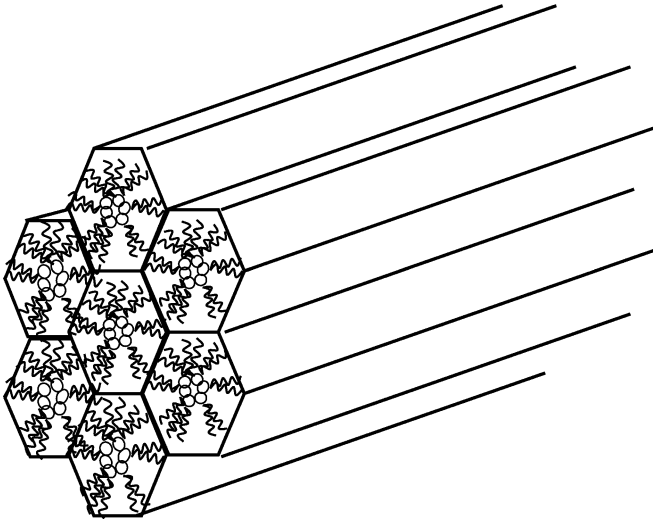

Fig. 11 Schematic representation of the typical bidimensional hexagonal structure of AOT liquid crystals

XPS spectra

The XPS spectra of composites containing cobalt(II), iron(II), and iron(III) are shown in Figs. 13, 14, and 15, respectively; the peak position and the full width at half maximum (FWHM) of these cations are collected in Table 4. For comparison, the XPS spectra of pure salts and the corresponding peak parameters have also been reported. In the cobalt-containing composite samples, two peaks (1 and 2) can be observed owing to the spin–orbit components of Co $2p_{3/2}$ and Co $2p_{1/2}$. The shoulders (1′ and 2′) can be attributed to secondary electronic processes accompanying the photoelectron expulsion (shake up). A system-specific binding energy of the cobalt-containing samples, which can be attributed to the peculiar coordination sphere surrounding the cobalt ions, is also noted. The lower value of the Co_{2p} binding energy obtained for the AOT complex relative to the pure $CoCl_2$ compound is indicative of an increase elec-

Table 3 Peak position and lattice parameters of pure AOT and salts/AOT

	2θ	d_{100}(Å)	2θ	d_{110}(Å)	2θ	d_{200}(Å)
Pure AOT	4.25	20.8	7.46	11.8	8.36	10.3
$CoCl_2$/AOT; $R=0.085$	4.09	21.6	–	–	–	–
$K_4Fe(CN)_6$/AOT; $R=0.051$	3.62	24.4	–	–	–	–
$K_3Fe(CN)_6$/AOT; $R=0.055$	3.62	24.4	5.92	14.9	7.06	12.5
Cobalt–iron(II) cyanide/AOT;$S=1$	4.20	21.0	7.21	12.3	8.35	10.6
Cobalt–iron(III) cyanide/AOT;$S=1$	4.20	21.0	7.20	12.3	8.18	10.8

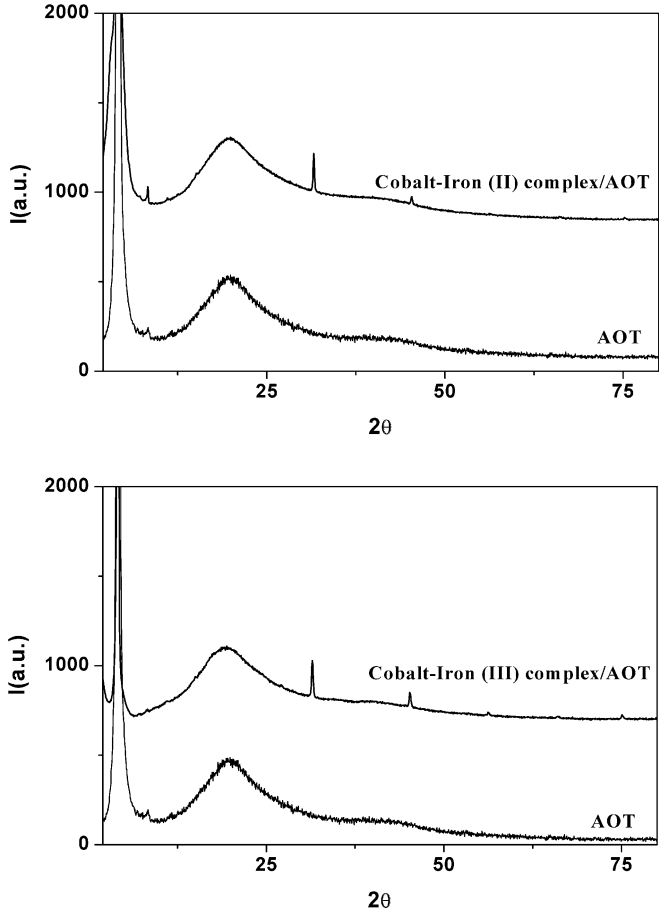

Fig. 12 Powder X-ray diffractograms of cobalt–iron cyanide complex/AOT ($S=1$) composites. The spectrum of pure AOT is also reported for comparison

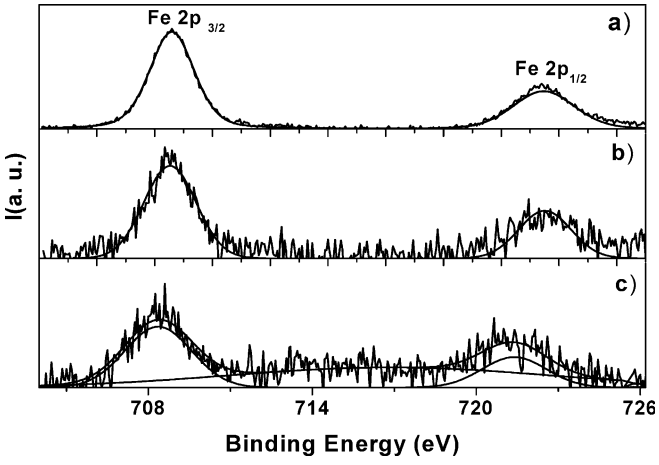

Fig. 14a–c Fe 2*p* XPS spectra of pure $K_4Fe(CN)_6$ (**a**), $K_4Fe(CN)_6$/AOT (**b**), and cobalt–iron(II)/AOT (**c**) composites. The *large band* in **c** is due to the emission of Co LMM Auger electrons

tronic charge on the cobalt centers with respect to the precursor [25].

Further contributions to the observed shift of the binding energy value with respect to pure $CoCl_2$ could arise from confinement and nanoparticle size effects [9].

The significant increase of the FWHM of the Co peak observed in cobalt–iron cyanide complex containing composites indicates the presence of different cobalt species. We have not found a reasonable explanation of this finding.

An inspection of the XPS spectra of iron(II)-containing samples leads to the conclusion that, independently on the sample composition, the Fe(II) ions are stable and the first coordination shell of Fe(II) is the

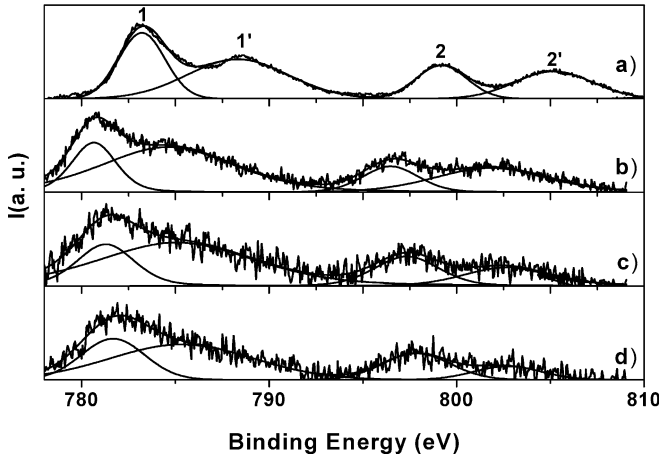

Fig. 13a–d Co 2*p* XPS spectra of pure $CoCl_2$ (**a**), $CoCl_2$/AOT at $R=0.133$ (**b**), cobalt–iron(II)/AOT at $S=0.5$ (**c**), and cobalt–iron(III)/AOT at $S=0.5$ (**d**) composites

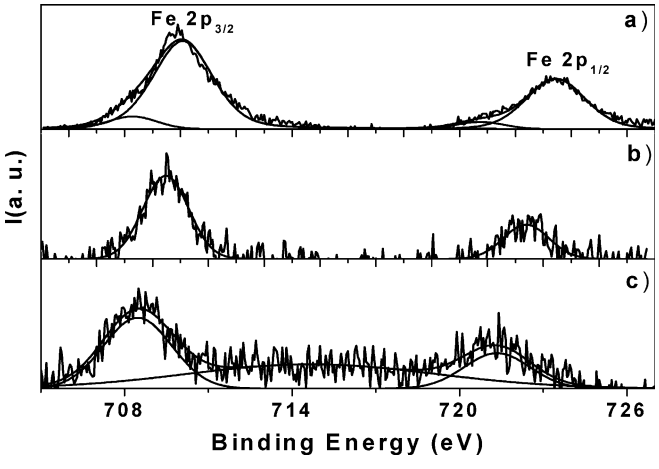

Fig. 15a–c Fe 2*p* XPS spectra of pure $K_3Fe(CN)_6$ (**a**), $K_3Fe(CN)_6$/AOT composite at $R=0.060$ (**b**) and cobalt–iron(III)/AOT composite at $S=0.5$ (**c**). The spectrum of the pure $K_3Fe(CN)_6$ exhibits a low-energy component attributed to Fe(II) and a high-energy component due to Fe(III). The spectra **b** and **c** exhibit only the low-energy component

Table 4 XPS binding energies (eV) and full width at half maximum (FWHM) of the most intense peaks

Samples	Fe $2p_{3/2}$		Co $2p_{3/2}$	
	BE[a](eV)	FWHM	BE[a](eV)	FWHM
$CoCl_2$			783.2	2.9
$K_4Fe(CN)_6$	708.6	1.9		
$K_3Fe(CN)_6$	709.9	2.4		
	708.4	1.6		
$CoCl_2$/AOT ($R=0.133$)			780.7	2.6
$K_4Fe(CN)_6$/AOT ($R=0.051$)	708.5	1.9		
$K_3Fe(CN)_6$/AOT ($R=0.060$)	708.4	1.7		
Cobalt–iron(II)/AOT complex ($S=0.5$)	708.3	2.2	781.4	3.4
Cobalt–iron(III) /AOT complex ($S=0.5$)	708.5	2.3	781.7	4.1

[a]The values of BE are referred to the energy of the C 1*s* set at 285.1 eV

same (i.e., the iron ions are always coordinated by cyanide groups). On the other hand, the comparison of the XPS spectra of iron(III)-containing samples strongly suggests that in these composites there is an X-ray-induced complete reduction of the iron(III) to iron(II) ions enhanced by the surfactant presence and/or confinement effects. This enhancement effect has been experimentally ascertained by collecting XPS spectra of pure $K_3Fe(CN)_6$ as a function of time. In this case, we observe a progressive but slow increase of the peak at 708.4 eV owing to Fe(II) at the expenses of that of Fe(III) at 709.9 eV [25].

Conclusions

This work proves that evaporation of volatile components (water and *n*-heptane) of salt-containing w/o microemulsions affords $CoCl_2$/AOT, $K_4Fe(CN)_6$/AOT, and $K_3Fe(CN)_6$/AOT composites containing nanoparticles. WAXS experiments show that these nanoparticles are very small and located in the hydrophilic region of the typical bi-dimensional hexagonal structure of AOT liquid crystals. Resuspension of the salt/AOT composites in dry *n*-heptane leads to stable dispersions of surfactant-coated salt nanoparticles. By SAXS, the presence of very small nanoparticles in the salt/AOT/*n*-heptane resuspended composites has been ascertained. By simple mixing of two dry dispersions of $CoCl_2$ and $K_4Fe(CN)_6$ or $K_3Fe(CN)_6$ nanoparticles in AOT/*n*-heptane solutions, very small $Co_x[Fe(CN)_6]$ nanoparticles via solid–solid reaction in the liquid phase at room temperature were synthesized. The cobalt–iron complex nanoparticle formation occurs rapidly and quantitatively through redistribution of the $CoCl_2$ and $K_4Fe(CN)_6$ or $K_3Fe(CN)_6$ among the dry AOT reversed micelles. Confinement effects and surfactant adsorption have been emphasized by UV-Vis and calorimetric measurements. Moreover, WAXS measurements of cobalt–iron complex/AOT composites indicate that nanoparticle size is significantly greater than that found in liquid samples, while XPS spectra allow us to put into evidence an X-ray-induced complete reduction of the iron(III) to iron(II) ions enhanced by the presence of surfactant and/or confinement effects.

Acknowledgements Financial support from Università di Palermo is gratefully acknowledged.

References

1. Calandra P, Longo A, Turco Liveri V (2003) J Phys Chem B 107:25–30
2. Calandra P, Longo A, Marcianò V, Turco Liveri V (2003) J Phys Chem B 107:6724–6729
3. Turco Liveri V (1999) Curr Top Colloids Interface Sci 3:65–74
4. Calandra P, Longo A, Turco Liveri V (2001) Colloid Polym Sci 279:1112–1117
5. Chow PY, Ding J, Wang XZ, Chew CH, Gan LM (2000) Phys Stat Sol A 180:547–553
6. Vesta CR, Zhang ZH (2002) Chem Mater 14:3817–3822
7. Ruland W (1974) J Appl Cryst 7:383–386
8. Feign LA, Svergun DI (1987) Structure analysis by small angle X-ray and neutron scattering. Plenum Press, New York
9. Giordano C, Longo A, Turco Liveri V, Venezia AM (2003) Colloid Polym Sci 281:229–238
10. Kitahara A, Kon-no K (1966) J Phys Chem 70:3394–3398
11. Nitsch W, Plucinski P (1990) J Coll Int Sci 136:338–351
12. Linke WF, Seidell A (1958) Solubilities of inorganic and metal organic coumpounds, vol 1. Van Nostrand, New York

13. Handbook of chemistry and physics, 67th edn (1986–1987) CRC Press, Boca Raton, FL
14. Eastoe J, Stebbing S, Dalton J, Heenan R (1996) Colloid Surf A 119:123–131
15. Sunamoto J, Hamada T (1978) Bull Chem Soc Jpn 51:3130–3135
16. Nicholls D (1973) Compr Inorg Chem 3:1025–1051
17. Naiman CS (1961) J Chem Phys 35:323–328
18. Bonner OD, Choi YS (1974) J Phys Chem 78:1723–1727
19. Onori G, Santucci A (1993) J Phys Chem 97:5430–5434
20. North AN, Dore JC, McDonald JA, Robinson BH, Heenan RK, Howe AM (1986) Colloids Surf 19:21–29
21. Mackeben S, Müller-Goymann CC (2000) Int J Pharm 196:207–210
22. Kotlarchyk M, Huang JS, Chen SH (1985) J Phys Chem 89:4382–4386
23. Hirai M, Kawai-Hirai R, Yabuki S, Takizawa T, Hirai T, Kobayashi K, Amemiya Y, Oya M (1995) J Phys Chem 99:6652–6660
24. Ekwall P, Mandell L, Fontell K (1970) J Coll Int Sci 33:215–235
25. Chastain (ed) (1992) Handbook of X-ray photoelectron spectroscopy. Perkin–Elmer, Eden Prairie, MN